Photonic band gap fiber accelerator

Xintian Eddie Lin*
Stanford Linear Accelerator Center, Stanford University, Stanford, California 94309
(Received 29 September 2000; published 31 May 2001)

There are three requirements in making a traveling wave accelerator: longitudinal electric field, synchronization, and confinement. We present and analyze a conceptually new kind of charged particle accelerator, making use of a photonic band gap lattice for field confinement near the beam axis, and employing dielectric material to produce a speed of light synchronous longitudinal electric field. An example structure design is presented. We also discuss nonlinear effect and other configurations without higher order dipole modes. Parallel scheme and fabrication are presented.

DOI: 10.1103/PhysRevSTAB.4.051301 PACS numbers: 41.75.Jv, 42.70.Qs

I. INTRODUCTION

Traditional microwave accelerators can be considered as metallic waveguides, which transport TM_{01} mode down the tube. Periodic disk loading slows the phase velocity of the wave to the speed of light (SOL), at which the relativistic particles are traveling. In analogy to a surfer riding on the comoving ocean wave, the synchronized longitudinal electric field achieves a sustained acceleration to charged particles over many wavelengths.

Scaling law indicates that, given the same amount of input power, smaller structures have higher fields and therefore higher accelerating gradients. This is the drive behind the gradual increase in microwave frequency in linear accelerators: SLAC 2 mile linac working at *S* band 2856 Hz; proposed Next Linear Collider (NLC) at *X* band 11.424 GHz; extensive research at *W* band (75–120 GHz) and even infrared. However, at higher frequency, the structure becomes correspondingly smaller, leading to difficulty in 3D machining. The higher order modes in the structure generate wakefields that perturb the trailing particles and cause instability. The short range transverse wakefield is proportional to the third power of the structure size, and thus becomes much worse at higher frequency. In fact, the proposed NLC design has to utilize detuning and manifold damping to control the wakefield. Another obstacle is the lack of good material to enclose electromagnetic fields at high frequency. For example, the attenuation length of 1 μm wavelength TM_{01} mode in a 2 μm copper tube is 0.7 mm, too short for an accelerator structure. Here we propose a different accelerator structure that addresses the aforementioned difficulties: It is based on dielectric waveguide and photonic band gap (PBG) material.

II. DIELECTRIC WAVEGUIDE ACCELERATOR (DWA)

It is well known that the wave in a hollow straight waveguide has phase velocity higher than the speed of light. Similar to periodic disk, dielectric lining in the waveguide has the effect of slowing down the phase velocity. Taking a tube of radius b, that is completely filled by material with dielectric constant $\epsilon_r > 1$, the longitudinal electric field of TM_{0m} mode is expressed by

$$E_z = E_0 J_0(k_r r) e^{-jk_z z}, \tag{1}$$

with $k_r = \sqrt{\epsilon_r k_0^2 - k_z^2} = j_{0n}/b$, where $k_0 = \omega/c$ and j_{0n} is the nth root of Bessel function J_0. The last equal sign comes from the boundary condition at $r = b$. The SOL phase velocity requirement $k_0/k_z = 1$ gives the synchronization frequency

$$k_0 = \frac{j_{0n}}{\sqrt{\epsilon_r - 1}\, b}. \tag{2}$$

One figure of merit, Z_c, relates the accelerating gradient E_0 and the input power P

$$Z_c \equiv \frac{E_0^2 \lambda^2}{P} = \left[\frac{2}{j_{0n} J_1^2(j_{0n})\pi}\right] \frac{(\epsilon_r - 1)^2}{\epsilon_r} \frac{(2\pi)^2}{j_{0n}} Z_0, \tag{3}$$

where λ is the wavelength and Z_0 is the vacuum impedance, about 377Ω. The factor in the square bracket approaches one when n goes to infinity and is off by only

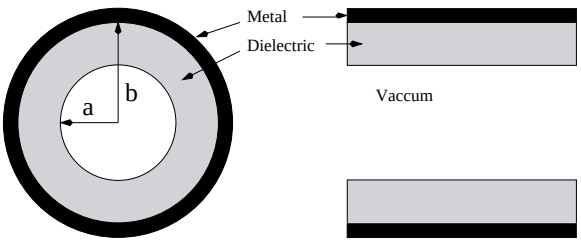

FIG. 1. Dielectric waveguide accelerator.

*Email address: eddie@slac.stanford.edu

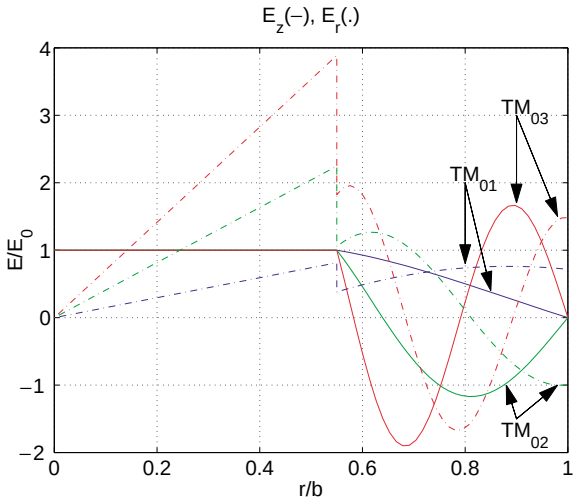

FIG. 2. (Color) Electric field distribution inside the DWA. Solid lines and dotted lines represent longitudinal and transverse electric fields, respectively.

2% even for $n = 1$. Obviously TM_{01} mode provides the highest accelerating gradient for a given amount of power.

To allow uninterrupted beam passage, a center hole through the dielectric core is necessary. Field solution of this configuration is available [1]. In the case of $\epsilon_r = 2.13$ and $a/b = 0.55$ (Fig. 1), the SOL frequencies $k_0 b$ are 2.96, 8.17, and 14.13 for TM_{01}, TM_{02}, and TM_{03} modes, respectively. Field distributions are illustrated in Fig. 2. The longitudinal electric field E_z is uniform inside the center hole, a direct result of the SOL phase velocity. The Maxwell's equation reduces to

$$\nabla_\perp^2 E_z = (k_0^2 - k_z^2) E_z = 0 \qquad (4)$$

inside the vacuum. Under $m = 0$ azimuthal variation, the only possible solution is $E_z(r) = \text{const}$. Even though $E_r \neq 0$, the radial force including that from H_ϕ for a relativistic particle vanishes. Therefore particles experience a uniform acceleration only in the z direction. From the material damage and wall loss point of view, TM_{01} mode is superior to other higher order monopole modes by virtue of its smaller magnetic field on the wall and smaller electric field in the dielectric.

The above dielectric waveguide accelerators (DWAs) have been tested in laboratory at C band (7.8 GHz) [2], and a planar version at W band (91 GHz) has also been tested [3].

III. PHOTONIC BAND GAP MATERIAL

We have pointed out that the metal at shorter wavelengths is too lossy to be an effective material to confine and transport electromagnetic (EM) waves. Yablonovitch [4] and John [5] proposed an artificial periodic lattice to prohibit EM waves from propagating. A photonic crystal is a periodic structure in one, two, or three dimensions. The multiple scattering of the electromagnetic wave in the periodic lattice may give rise to a forbidden energy gap, over which EM waves cannot propagate. This phenomena is in analogy to the electron band gap formation inside semiconductor materials. A familiar example in one dimension is the multilayer coating on a dielectric mirror. Because dielectric has extremely low loss, PBG material can replace metal as a perfect reflector.

The simplest approach is to replace the metal in Fig. 1 by a multilayer coating. Fink *et al.* [6] demonstrated infrared guiding in air with a multilayer structure made by tellurium and polystyrene. Alternatively, one could replace the metal with two- or three-dimensional photonic crystal that has band gap at appropriate frequency. Single mode guiding in two-dimensional close packed hexagonal lattice has been demonstrated in the visible over 40 mm [7]. A three-dimensional photonic crystal at infrared has also been fabricated on a 6 in. silicon wafer [8].

We choose the two-dimensional hexagonal lattice based on the manufacturing process and the material's high breakdown threshold, which will be discussed in later sections.

A different approach is taken by Smith *et al.* [9] to use a 2D PBG lattice made of metal to replace the sidewall of the disk-loaded waveguide. The resulting 3D structures are difficult to scale to small dimensions and still share the high losses at high frequency.

A. PBG

A 2D PBG has a periodic structure in the x-y plane and is uniform in the z direction. Earlier studies [10,11] concerned in-plane propagation, in which the wave has no variation in the z direction. Recently, more studies [7,12–14] have concentrated on using 2D PBG to transport light. However, the application in accelerators requires an energy band gap at SOL phase propagation, i.e.,

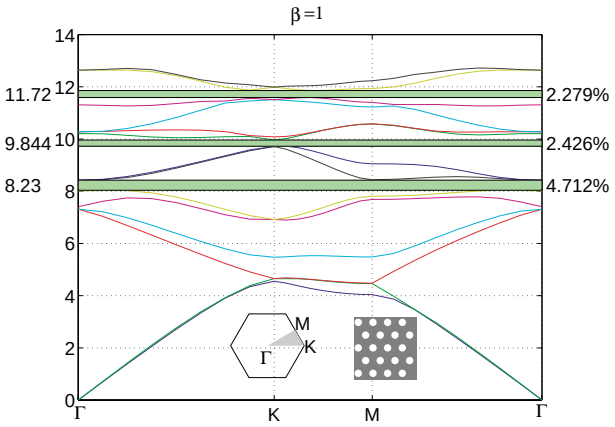

FIG. 3. (Color) Photonic band gaps in 2D. The band diagram is plotted over the irreducible Brillouin zone, highlighted in light gray. A section of the periodic structure is also illustrated, with silica in gray and air in white. The green regions in the plot are the band gaps. Midgap values and gap/midgap ratios are displayed on the left and right of the band, respectively.

band gap around $k_0 = k_z$. Figure 3 illustrates such band gaps in a particular 2D lattice composed of silica and air. The gray area is fused silica ($\epsilon_r = 2.13$); the air cylinder (white) forms the triangular lattice. Maxwell's equations are solved by plane wave method (PWM) [15,16] with $\beta = k_z/k_0 = 1$. In the simulation, 469 plane waves are used. Convergence studies show that band center frequencies are accurate to better than 1% relative, and the gap to midgap ratio is better than 0.1% absolute. The radius of the air rod is $r = 0.35a$, with a the inter-rod distance. The lowest SOL band gap centers at $k_0 = 8.23$, where k_0, k_z are normalized to $1/a$. It is evident that there are several SOL band gaps. For accelerator applications, it would be ideal to have only one such gap that is utilized to trap the fundamental mode for acceleration, and let all other higher order modes leak out to reduce instabilities. We will show such a configuration in a later section.

B. Defect mode

The defect mode, introduced by making a defect in a perfect lattice, can be guided if the frequency is within the band gap. One realization is illustrated in Fig. 4. The frequency and field distribution are calculated by employing a supercell that includes the volume of 108 unit cells, and appropriate symmetry is taken to reduce the size of the numerical computation. With the radius of the center hole $r_0 = 0.52a$, the frequency of the defect mode, $k_0 = k_z = 8.20$, falls within the lowest SOL band gap. The mode is a TM_{0n}-like mode with longitudinal electric field uniform inside the center defect. The rapid oscillation of E_z inside the center defect is an artifact of finite number (18 per unit cell) of plane waves included in the calculation. The field outside the core decays steadily at about 6 dB per unit cell in the x direction. The different

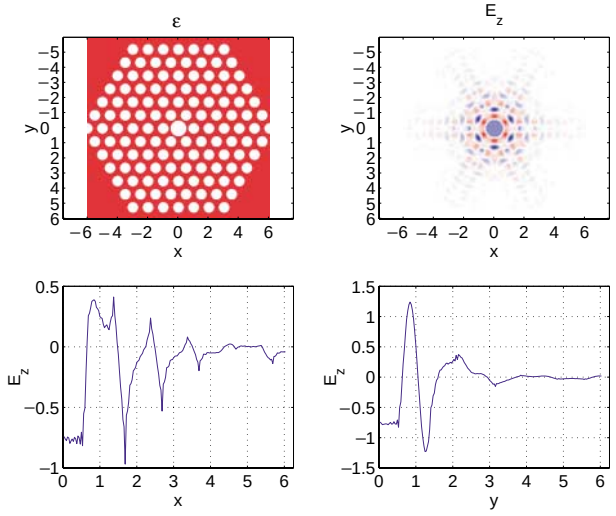

FIG. 4. (Color) The dielectric distribution and the field distribution of the defect mode trapped by 2D PBG fiber. In the top right plot, blue and red represent negative and positive values, respectively.

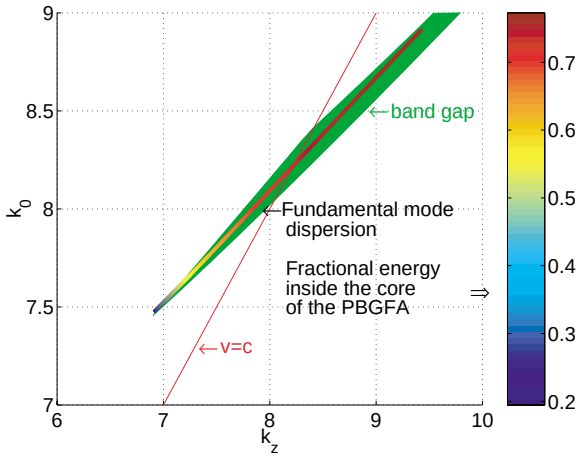

FIG. 5. (Color) The dispersion of the defect mode. The green band is the band gap responsible for localization. The dispersion curve is color coded by the energy fraction inside the core of the PBG fiber.

decay lengths in the x and y directions are a result of different coupling strengths in the respective direction. Due to the field penetration, part of the PBG material acts as the dielectric lining in Fig. 1. A simplistic DWA model of one free parameter $a/b = 0.55$ gives synchronized TM_{02} mode at $k_0 = 8.17$ and $v_g/c = 0.60$, which compare very well with the simulation: $k_0 = 8.20$ and $v_g/c = 0.58$.

The dispersion of the defect mode is plotted in Fig. 5. The band gap is in green and the SOL line is in red. The dispersion curve is color coded with the fractional energy inside the core of the PBG fiber. We artificially defined the core as the area within two lattice spacings of the center. In particular, the synchronized defect mode has about 73% of the stored energy inside the core, signifying a strongly trapped mode.

IV. PBG FIBER ACCELERATOR (PBGFA)

One interesting feature of electromagnetism in dielectric media is that there is no fundamental length scale other than the assumption that the system is macroscopic. Therefore, we are free to choose the wavelength that is convenient. One good starting point is at $\lambda = 1$ μm, where the optical source and techniques are mature, and fused silica is relatively easy to manufacture and can stand a high damage threshold. We will mention some scaling results that provide design at other, perhaps more desirable, wavelengths.

Because of the pulse shape slippage with respect to the relativistic beam, pulse length has to be longer than $(1 - v_g/c)l/c$, where l is the structure length. For a 10 cm long structure, $\tau > 140$ ps. In this pulse length regime, the damage is thermal diffusion limited, therefore the damage fluence increases as $\tau^{1/2}$. The damage threshold of 1.053 μm laser is about $F = 17$ J/cm^2 on bulk fused silica [17], which corresponds to a peak electric field

$$E_{th} = \sqrt{\frac{2F}{\sqrt{\epsilon_r}\,\tau}}\,Z_0 \tag{5}$$

of 0.79 GeV/m. The simulation indicates that the peak electric field inside the dielectric material is 2.1 times that of the center electric field. Therefore, the accelerating gradient will be limited to $E_0 = 0.38$ GeV/m. Dielectric loss is ignored in the following calculation.

From the longitudinal impedance $Z_c = 19.5\Omega$ (an equivalent of $R/Q = 0.6\Omega$ on a $2\pi/3$ cell) obtained in the simulation, we can find out the power

$$P = \frac{E_0^2\lambda^2}{Z_c} = 7.4 \text{ kW} \tag{6}$$

needed to produce the gradient, which translates to a $U = 1.0$ μJ pulse. Beam loaded gradient

$$E_0^l = E_0 - \frac{1}{4}\frac{qcZ_c}{\lambda^2}\frac{1}{1 - v_g/c} \tag{7}$$

equals half of unloaded gradient E_0 at maximum energy transfer. The charge q is assumed to be a point charge, and the fundamental theorem of beam loading [18] is used. The optimal charge

$$q_{op} = \frac{U}{\frac{1}{2}E_0 l} = (1 - v_g/c)\,\frac{2E_0\lambda^2}{Z_c c} \tag{8}$$

corresponds to 3.4×10^5 electrons accelerated at a loaded gradient of 0.19 GeV/m. It is worth noting that the laser power and thus optimal beam loading scales with wavelength to the second power, therefore more charge (1.4×10^6 electrons) can be accelerated at 2 μm wavelength. Due to extreme loss from IR absorption, a wavelength longer than 2 μm can hardly be transported in silica. Another approach to increase the charge is through parallel PBG fiber accelerators (PBGFAs), a section of which is illustrated in Fig. 6. Focusing of an individual beamlet is difficult to implement in traditional magnet design. A guided quadrupole defect mode, with a phase velocity slightly different from the speed of light, may be utilized. Alternatively, a rectangular defect inducing enough quadrupole moment for the fundamental accelerator mode can be used [19]. But alternating structure orientation is needed to create a FODO lattice. Later, we will describe the manufacture process that is compatible with making such bundles. Designing a PBGFA at 10 μm wavelength is also attractive, but we need to study another dielectric material, chalcogenide glass, for example.

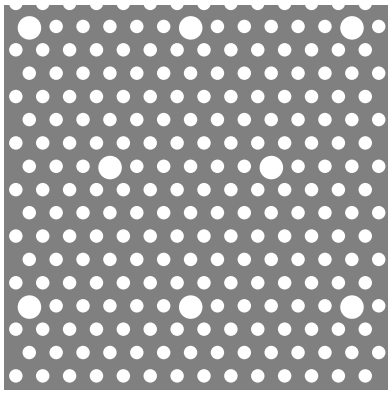

FIG. 6. A section of a parallel PBGFA bundle.

A. Nonlinear effect

Under such high electric field, self-phase modulation from nonlinear effect plays an important role. The nonlinear refraction is characterized by an intensity-dependent refractive index following [20]

$$n = n_0 + n_2|E|^2, \tag{9}$$

where n_0 is the refractive index in the linear regime and n_2 is the nonlinear index coefficient, which takes the value of $n_2 = 1.22 \times 10^{-22}$ $(\text{V/m})^{-2}$ for silica. From perturbation theory, the frequency shift due to slight change of dielectric constant is

$$\frac{\delta\omega}{\omega_0} = -\frac{1}{2}\frac{\int_{V'}\langle\delta\epsilon_r\rangle|E|^2\,dV}{\int_V \epsilon_r|E|^2\,dV} = -\frac{1}{2}\,n_0 n_2 f E_0^2, \tag{10}$$

where V' and V are the volume of the dielectric and the total volume, respectively. The averaged dielectric constant perturbation $\langle\delta\epsilon_r\rangle = n_0 n_2|E|^2$ is used, and the field weighted filling fraction

$$f = \frac{\int_{V'}|E|^4\,dV}{E_0^2\int_V \epsilon_r|E|^2\,dV} \tag{11}$$

is found to be 0.4 from simulation. To reestablish the SOL synchronization, the laser frequency needs to be detuned (Fig. 7) by

$$\Delta\omega/\omega_0 = \frac{\delta\omega/\omega_0}{1 - v_g/c} = -1.2 \times 10^{-5}, \tag{12}$$

with $E_0 = 0.38$ GeV/m. Without such detuning, the accumulated phase error would be

$$\delta\phi = \frac{\delta\omega}{\omega_0}\,\frac{k_z l}{v_g/c} = -5.6 \text{ rad}. \tag{13}$$

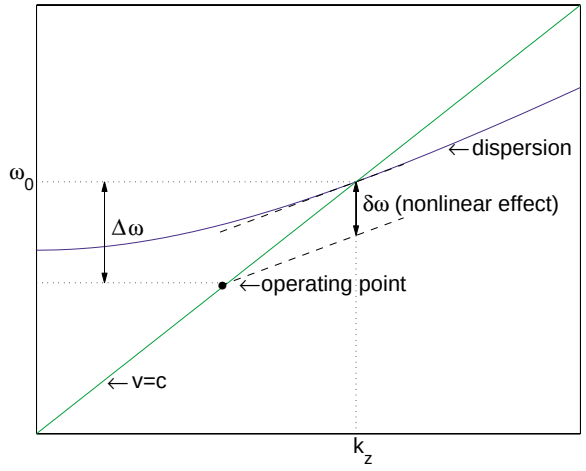

FIG. 7. (Color) Frequency detuning due to nonlinear effect.

Another nonlinear effect is stimulated Raman scattering (SRS), which turns the input photons to photons at a lower frequency (Stokes lines). The Raman threshold, defined as the input pump power at which the Stokes power becomes equal to the pump power at the fiber output, is given by [9]

$$P_0^{cr} = \frac{16}{g_R}\frac{A_{\text{eff}}}{l}, \tag{14}$$

where A_{eff} is the effective fiber area and g_R is the Raman gain. Using the measured value of $g_2 = 1 \times 10^{-13}$ m/W, and an estimated fiber area $A_{\text{eff}} = 12\ \mu\text{m}^2$ from Fig. 4 ($a = 1.3\ \mu$m, assume a core radius of 2 lattice spacing, and 44% air filling fraction), we obtain the threshold power $P_0^{cr} = 19$ kW, which is substantially higher than the input power (7.4 kW).

Another nonlinear effect, the stimulated Brillouin scattering, is less important than SRS with short pulses ($t <$ 1 ns) [21].

B. Higher order dipole mode free

The number of SOL band gaps in the above PBG material is shown in Fig. 8. From the fundamental band gap to 4 times its frequency, about 6% of the spectrum space is covered by other band gaps, which makes it susceptible to trapping other defect modes. And numerical simulation has shown that this is the case: some dipole modes are localized by the band gaps. The high frequency and wide band gap at 8.23 enhance the chances of localization: The mode density is proportional to frequency at high frequency, and the chance of a dipole mode frequency being within the band gap is proportional to the band gap width. To avoid that, we also investigated another lattice, the so-called honeycomb lattice. It is formed by taking 1/3 of the air rods out of the existing triangular lattice, shown in Fig. 9. At $r/a = 0.24$, it has SOL band gaps at $k_0 = 4.579$ and 19.69 with the higher one extremely narrow. The lower frequency band gap localizes a monopole defect mode formed by replacing the center six air rods

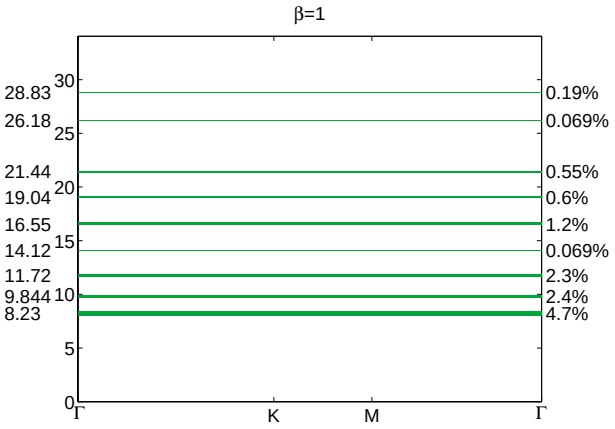

FIG. 8. (Color) Photonic band gaps within the lower 100 modes. For clarity, frequency bands are omitted; only the band gaps are plotted along with their gap/midgap ratio.

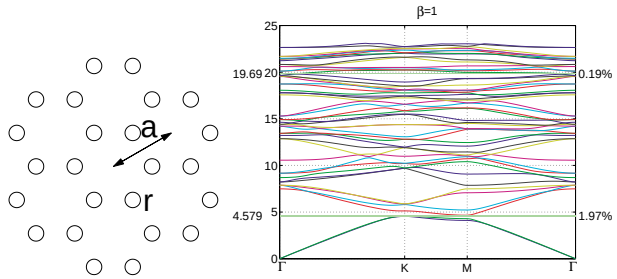

FIG. 9. (Color) Honeycomb lattice and its SOL band gap. In the simulation, we assumed $r/a = 0.24$ and k_0 is normalized to $1/a$.

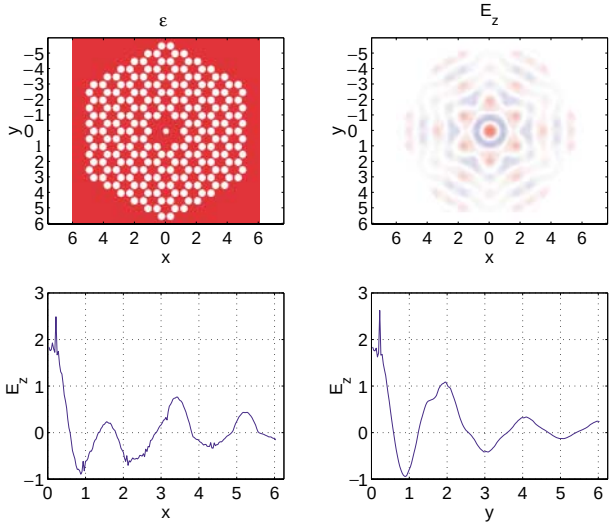

FIG. 10. (Color) Defect mode in a honeycomb lattice.

with a $r_0/a = 0.19$ one, as illustrated in Fig. 10. The defect mode has $k_0 = k_z = 4.56$. The simulation also shows no trapped dipole modes in the lowest band gap. We did not check the higher band gap at 19.69 because of the computation time involved, but we believe it will not cause any adverse effect based on the band gap width.

C. Pulse injection

Coupling laser power, usually in TEM mode, into accelerator structure is a subject in its own right. One way to couple light into a structure is through a coupler cell, similar to the traditional microwave version in turning TE_{10} waveguide mode to TM_{01} cavity mode. Alternatively, a radially polarized laser beam can be focused by an axicon [22] to yield the right symmetry and longitudinal electric component to inject into the fiber mode.

D. Manufacture

A fused silica bundle like that in Fig. 4 has been manufactured with the drawing method [7,23]: Stacks of fiber tubes are bundled and repeatedly pulled down to desired dimensions. Pitch dimensions a from 53 nm to 2 μm are

achieved. Interstitial holes can be introduced by stacking cylindrical tubes instead of hexagon-shaped canes. The multiple stack and draw process is especially suitable in massive production of PBGFA structures; kilometers of PBG fiber have been made. The inexpensive manufacture process is compatible with making multiple parallel linac bundles.

V. CONCLUSION

We have presented a schematic design of a silica-based PBGFA structure that is able to reach 0.4 GeV/m gradient, and is relatively easy to manufacture. To our knowledge, this is the first numerical demonstration that 2D PBG supports accelerator mode. With its many advantages, PBGFA is a promising scheme that is worth further investigation.

Even though we have demonstrated many aspects of PBGFA, the above examples are by no means optimal. More work needs to be done on PBG material engineering that produces lower frequency SOL band gap, suitable gap/midgap ratio. Defect modes with smaller field inside dielectric and higher beam loading are beneficial. A defect mode with quadrupole components to focus the electron beam is essential in maintaining beam stability and making multiple parallel accelerator possible. Pumping the tiny tubes to a high vacuum is another challenge. Further research into longer laser wavelength (for example, 10.6 μm) will benefit structure alignment, beam loading, and manufacture tolerance, but its ultimate fate lies in the material's high damage threshold.

APPENDIX A: DIELECTRIC WAVEGUIDE ACCELERATOR

Considering a metal pipe completely filled by a dielectric material with dielectric constant ϵ_r, the fields of TM_{0n} modes can be written as

$$E_z = E_0 J_0(k_r r) e^{-jk_z z}, \tag{A1}$$

$$E_r = j\,\frac{\beta}{\sqrt{\epsilon_r - \beta^2}}\,E_0 J_1(k_r r) e^{-jk_z z}, \tag{A2}$$

$$H_\phi = j\,\frac{\epsilon_r}{\sqrt{\epsilon_r - \beta^2}}\,\frac{E_0}{Z_0}\,J_1(k_r r) e^{-jk_z z}, \tag{A3}$$

where a time harmonic expression $e^{jk_0 ct}$ is omitted for brevity. The propagation constant $k_z = k_0/\beta$, and Z_0 is the vacuum impedance, about 377Ω. For a SOL propagation, $\beta = 1$, which gives the synchronization frequency $k_0 = j_{0n}/\sqrt{\epsilon_r - 1}\,b$ from the boundary condition at $r = b$. The j_{0n} is the nth root of the Bessel function $J_0(x)$. From the dispersion relations

$$k_0 = \sqrt{k_z^2 + k_r^2}/\epsilon_r \tag{A4}$$

we obtain the group velocity

$$\frac{v_g}{c} = \frac{dk_0}{dk_z} = \frac{1}{\epsilon_r} \tag{A5}$$

at the synchronization. Another important figure of merit is the longitudinal impedance relating accelerating gradient E_0 with the input power P

$$Z_c \equiv \frac{E_0^2\lambda^2}{P} = \frac{E_0^2\lambda^2}{\int_0^b E_r H_\phi 2\pi r\,dr} = \left[\frac{2}{j_{0n}J_1^2(j_{0n})\pi}\right]\frac{(\epsilon_r - 1)^2}{\epsilon_r}\,\frac{(2\pi)^2}{j_{0n}}\,Z_0\,. \tag{A6}$$

The longitudinal impedance Z_c is a functional of the geometry and independent of the length scale and loss. Including the attenuation constant

$$\alpha \equiv \frac{dP/dz}{2P} = \frac{2\pi}{\lambda}\,\frac{\sqrt{\epsilon_r - 1}\,\epsilon_r}{j_{0n}}\,\frac{R_s}{Z_0} + \frac{2\pi}{\lambda}\,\frac{\epsilon_r \tan\delta}{2} \tag{A7}$$

limits only the optimal accelerating structure length. The first term accounts for the loss on the metal wall—the skin resistance $R_s = \sqrt{k_0 Z_0/2\sigma}$ from the finite conductivity σ. The second term is a result of dielectric loss tangent $\tan\delta$.

A direct comparison with disk loaded traveling wave linac of ϕ phase advance per cell is possible if we compare a cell with a section of DWA that is ϕ/k_0 long. The elasticity, defined as

$$\frac{R}{Q} \equiv \frac{V^2}{\omega U} \tag{A8}$$

for each cell, has an equivalent definition in DWA

$$\frac{R}{Q} = Z_c\,\frac{\phi}{(2\pi)^2}\,\frac{v_g}{c}\,. \tag{A9}$$

The equivalent quality factor

$$Q = \frac{k_0}{2\alpha v_g/c} \tag{A10}$$

also follows.

APPENDIX B: PLANE WAVE METHOD

We use the plane wave method to solve the following 2D equation

$$\nabla_t \times \left(\frac{1}{\epsilon_r}\,\nabla_t \times \vec{H}_t\right) - \frac{1}{\epsilon_r}\,\nabla_t(\nabla_t \cdot \vec{H}_t) - \left(k_0^2 - \frac{k_z^2}{\epsilon_r}\right)\vec{H}_t = 0 \tag{B1}$$

on the transverse components of magnetic field $\vec{H}_t$, where a harmonic dependence of $e^{-ik_0 ct + ik_z z}$ is assumed. This particular formulation has the advantage of being free of spurious modes in finite elements calculation [24]. The transverse distributions are expanded in terms of plane waves

$$\frac{1}{\epsilon_r(\vec{x})} = \sum_{\vec{G}} \kappa(\vec{G}) e^{i\vec{G}\cdot\vec{x}}, \tag{B2}$$

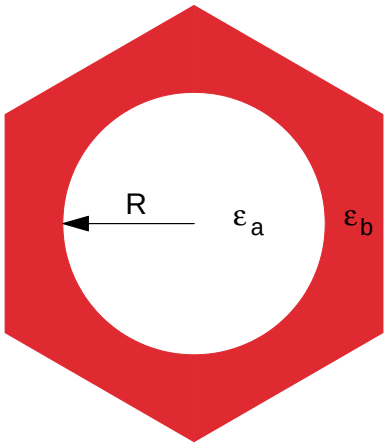

FIG. 11. (Color) Cylinder in a unit cell.

$$H_{x,\vec{k}}(\vec{x}) = e^{i\vec{k}\cdot\vec{x}} \sum_{\vec{G}} \tilde{H}_{x,\vec{k}}(\vec{G}) e^{i\vec{G}\cdot\vec{x}}, \tag{B3}$$

$$H_{y,\vec{k}}(\vec{x}) = e^{i\vec{k}\cdot\vec{x}} \sum_{\vec{G}} \tilde{H}_{y,\vec{k}}(\vec{G}) e^{i\vec{G}\cdot\vec{x}}, \tag{B4}$$

where $\vec{G}$ is the reciprocal lattice and $\vec{k}$ labels the field solution. After substituting the above expansions in Eq. (B1), we obtain the following matrix equation

$$\begin{pmatrix} K_{xx} & K_{xy} \\ K_{yx} & K_{yy} \end{pmatrix} \begin{bmatrix} \tilde{H}_{x,\vec{k}}(\vec{G}') \\ \tilde{H}_{y,\vec{k}}(\vec{G}') \end{bmatrix} = k_0^2 \begin{pmatrix} B_{xx} & 0 \\ 0 & B_{yy} \end{pmatrix} \begin{bmatrix} \tilde{H}_{x,\vec{k}}(\vec{G}') \\ \tilde{H}_{y,\vec{k}}(\vec{G}') \end{bmatrix} \tag{B5}$$

with

$$K_{xx} = \kappa(\vec{G} - \vec{G}')[(k_y + G'_y)(k_y + G_y) + (k_x + G'_x)(k_x + G'_x)], \tag{B6}$$

$$K_{xy} = \kappa(\vec{G} - \vec{G}')[-(k_x + G'_x)(k_y + G_y) + (k_y + G'_y)(k_x + G'_x)], \tag{B7}$$

$$K_{yx} = \kappa(\vec{G} - \vec{G}')[-(k_y + G'_y)(k_x + G_x) + (k_x + G'_x)(k_y + G'_y)], \tag{B8}$$

$$K_{yy} = \kappa(\vec{G} - \vec{G}')[(k_x + G'_x)(k_x + G_x) + (k_y + G'_y)(k_y + G'_y)], \tag{B9}$$

$$B_{xx} = \delta_{\vec{G}\vec{G}'} - \beta^2 \kappa(\vec{G} - \vec{G}'), \tag{B10}$$

$$B_{yy} = B_{xx}, \tag{B11}$$

where $\beta = k_z/k_0$. For numerical calculation, a finite number of N reciprocal lattice points $\vec{G}$ in Eq. (B5) are kept, making it a rank $2N$ generalized eigenvalue problem.

For a cylinder in a unit cell, shown in Fig. 11, the dielectric constant expansion can be obtained

$$\kappa(\vec{G}) = \begin{cases} \frac{1}{\epsilon_a} f + \frac{1}{\epsilon_b}(1 - f) & \text{if } \vec{G} = 0, \\ (\frac{1}{\epsilon_a} - \frac{1}{\epsilon_b}) f \frac{2J_1(|\vec{G}R|)}{|\vec{G}R|} & \text{if } \vec{G} \neq 0, \end{cases} \tag{B12}$$

where f is the fractional area of the cylinder in the unit cell and J_1 is the Bessel function.

[1] E. Marcatili and R. Schmeltzer, Bell Syst. Tech. J. **43**, 1783 (1964).
[2] M. E. Conde *et al.*, in *Advanced Accelerator Concepts: 8th Workshop*, edited by Wes Lawson, AIP Conf. Proc. No. 472 (AIP, New York, 1999), pp. 626–634.
[3] M. E. Hill, C. Adolphsen, W. Baumgartner, R. C. Callin, X. E. Lin, M. Seidel, T. Slaton, and D. H. Whittum, SLAC Report No. SLAC-PUB 8680, http:www.slac.stanford.edu/cgi-wrap/getdoc/slac-pub-8680.pdf.
[4] E. Yablonovitch, Phys. Rev. Lett. **58**, 2059 (1987).
[5] S. John, Phys. Rev. Lett. **58**, 2486 (1987).
[6] Y. Fink, D. J. Ripin, S. Fan, C. Chen, J. D. Joannopoulos, and E. L. Thomas, J. Lightwave Technol. **17**, 2039 (1999).
[7] R. Cregan, B. J. Mangan, J. C. Knight, T. A. Birks, P. Russel, P. J. Roberts, and D. C. Allan, Science **285**, 1537 (1999).
[8] S. Lin, J. Fleming, D. Hetherington, B. Smith, R. Biswas, K. Ho, M. Sigalas, W. Zubrzycki, S. Kurtz, and J. Bur, Nature (London) **396**, 251 (1998).
[9] R. G. Smith, Appl. Opt. **11**, 2489 (1972).
[10] M. Plihal and A. Maradudin, Phys. Rev. B **44**, 8565 (1991).
[11] R. Meade, K. Brommer, A. M. Rappe, and J. Joannopoulos, Appl. Phys. Lett. **61**, 495 (1992).
[12] T. Birks, P. Roberts, P. Russell, D. Atkin, and T. Shepherd, Electron. Lett. **31**, 1941 (1995).
[13] J. Knight, T. Birks, P. Russell, and D. Atkin, Opt. Lett. **21**, 1547 (1996).
[14] J. Knight, J. Broeng, T. Birks, and P. Russell, Science **282**, 1476 (1998).
[15] K. Leung and Y. Liu, Phys. Rev. Lett. **65**, 2646 (1990).
[16] Z. Zhang and S. Satpathy, Phys. Rev. Lett. **65**, 2650 (1990).
[17] B. C. Stuart, M. D. Feit, A. M. Rubenchik, B. W. Shore, and M. D. Perry, Phys. Rev. Lett. **74**, 2248 (1995).
[18] P. Wilson, in *Physics of High Energy Particle Accelerators*, edited by R. A. Carrigan, F. R. Huson, and M. Month, AIP Conf. Proc. No. 87 (AIP, New York, 1982), pp. 450–563.
[19] W Schnell and I. Wilson, in *Proceedings of the 1991 IEEE Particle Accelerator Conference, San Francisco* (IEEE, Piscataway, NJ, 1991), p. 3237.
[20] R. H. Stolen and C. Lin, Phys. Rev. A **17**, 1448 (1978).
[21] G. P. Agrawal, *Nonlinear Fiber Optics* (Academic, New York, 1989).
[22] R. D. Romea and W. D. Kimura, Phys. Rev. D **42**, 1807–1818 (1990).
[23] R. J. Tonucci, B. L. Justus, A. J. Campillo, and C. E. Ford, Science **258**, 783 (1992).
[24] J. Jin, *The Finite Element Method in Electromagnetics* (Wiley, New York, 1993).